PIER M

(Received 24 July 2024, Accepted 20 August 2024, Scheduled 12 September 2024)

A Compact High-Isolation Tri-Band MIMO Antenna Based on Characteristic Mode Analysis

Jinrong Su[1,*], Shiqi Di[1], Chunhui Yao[2], and Xinwei Chen[1]

[1] *School of Physics and Electronic Engineering, Shanxi University, Taiyuan 030006, China*
[2] *China North Industries North Automatic Control Technology Research Institute, Taiyuan, China*

ABSTRACT: This paper presents a compact 3-port multiple-input multiple-output (MIMO) antenna for 5G wireless communication, covering the 2.6 GHz, 3.5 GHz, and 4.8 GHz bands. Three orthogonal modes (TM_{10}, TM_{01}, and TM_{20} modes) are excited to realize tri-band operation and high isolation simultaneously. Using characteristic mode analysis (CMA), dual-slot structures and I-shaped patches are introduced to block coupling path, and the isolation is improved. Simulated and measured results show that the proposed antenna operates in the frequency bands of 2.57 to 2.64 GHz, 3.4 to 3.5 GHz, and 4.8 to 4.9 GHz with isolation better than 20.6 dB. In addition, it can be calculated that Envelope Correlation Coefficient (ECC) (< 0.06), Diversity Gain (DG) (> 9.99 dB), Total Active Reflection Coefficient (TARC) (< -10 dB), and Channel Capacity Loss (CCL) (< 0.45 bits/Hz/sec) are in acceptable level, implying excellent diversity performance and data transmission quality. It is worth noting that the evolution of the antenna is entirely based on the CMA, which greatly simplifies the design process. The antenna has the advantages of high isolation, compact structure, easy processing, and low cost, positioning it as a compelling candidate for integration into 5G wireless communication systems.

1. INTRODUCTION

The development of the fifth-generation (5G) wireless communication technology has raised higher demands on data transmission rates and throughput in wireless communications. Multiple-input multiple-output (MIMO) technology can significantly enhance channel capacity such that it has been widely adopted in 5G communication systems [1]. MIMO antennas are indispensable components in MIMO systems, and their performance and structure have an important impact on communication quality and the miniaturization of devices. One of the challenges in MIMO antenna design is how to reduce the mutual coupling between antenna elements within a limited space.

Various methods have been reported to enhance isolation. For example, coupling suppression is an effective method, with primary implementation approaches including defected ground structure (DGS) [2], and metamaterials [3, 4]. Coupling cancellation is another method achieved by introducing additional coupling paths to counteract the original coupling. For instance, decoupling networks [5, 6], neutralization lines [7, 8], and parasitic elements [9, 10] are all part of this category. In addition, hybrid decoupling methods are also reported [11, 12]. For example, in [11], a Z-shaped slot and short-circuit pins are introduced simultaneously, and more than 30 dB isolation is achieved. Abundant results have proven that these methods can effectively improve isolation. However, traditional antenna design relies on the designers' experience and iterative simulations, making the optimization process complex and time-consuming.

Characteristic modes analysis (CMA) evaluates an antenna's radiation and coupling modes at a fundamental physical level, which can reduce the number of iterations and promote design efficiency. According to literature reports, self-decoupling is achieved through CMA, including mode cancellations [13], exciting orthogonal modes [14], utilizing null-field region [15], and mode diversity [16]. The self-decoupling is ingeniously designed and structurally simple, but the antenna size is relatively large. To further miniaturize the antenna, some researchers have combined CMA with other decoupling methods. For example, in [17], CMA is used to determine the position of DGS, and a minimum isolation of 25 dB is achieved. In [18], a stepped electromagnetic bandgap combined with DGS and stub is introduced to reduce coupling by CMA. In [19–21], CMA is used to design the antenna element firstly, and then decoupling network [19], layout optimization [20] or shorting pins [21] are designed to reduce coupling. These methods have achieved satisfactory decoupling effects, and yet, most of their decoupling designs still use traditional approaches. Therefore, it is worth further exploration to implement decoupling using the CMA method.

In this paper, a compact tri-band 3-port MIMO antenna is proposed based on CMA. By simultaneously exciting three orthogonal modes of TM_{10}, TM_{01}, and TM_{20}, the antenna achieves tri-band operation. Additionally, CMA is further applied to analyze the coupling mode and help introducing a dual-slot DGS and I-shaped patch to improve the isolation. Compared with the current MIMO antenna using CMA, this work realizes tri-band operation and high isolation with small size and simple process. Tri-band operation supports a variety of applications including 4G Long-Term Evolution (LTE), 5G mid-

* Corresponding author: Jinrong Su (sujinrong@sxu.edu.cn).

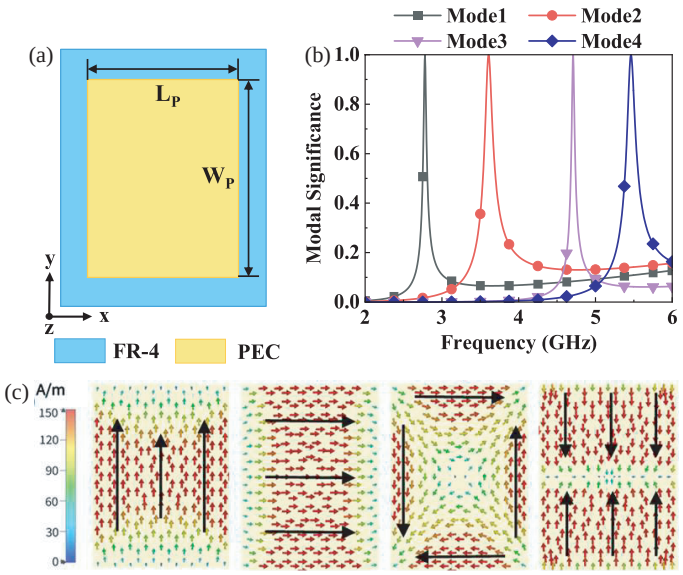

FIGURE 1. (a) Top view of the conventional patch, and (b) the corresponding MS curves and (c) characteristic current distributions of Mode 1 to Mode 4.

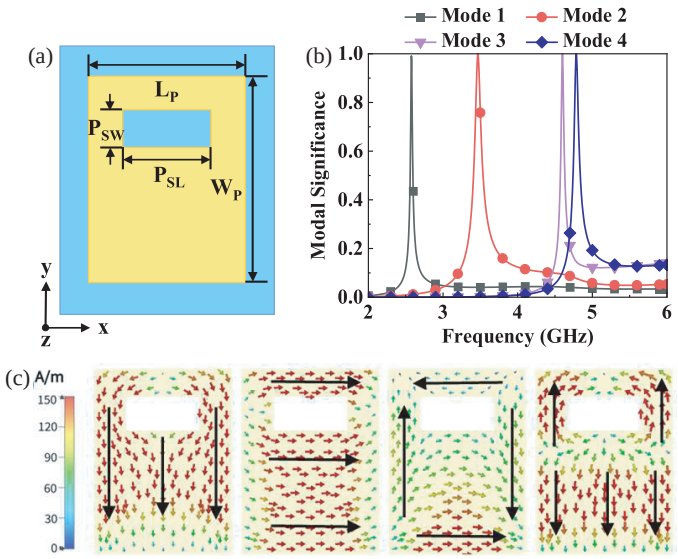

FIGURE 2. (a) Top view of the patch with slot, and (b) the correspondence MS curves and (c) characteristic current distributions of Mode 1 to Mode 4.

band applications, Wireless Local Area Network (WLAN), and Internet of Things (IoT).

2. DESIGN OF THE TRI-BAND ANTENNA BASED ON CMA

The following section introduces the antenna design based on the CMA, which includes the evolution from a single-port to a 3-port MIMO antenna, ultimately achieving high isolation. The modeling, simulation, and analysis of the antenna are conducted using electromagnetic simulation software ANSYS HFSS and CST Microwave Studio. In the simulation, a 1.6 mm thick FR-4 with a relative permittivity (ε_r) of 4.4 and a loss tangent ($\tan\delta$) of 0.02 is used as substrate.

2.1. Design of Antenna Element Using CMA

Figure 1 illustrates a conventional rectangular patch structure and its MS and characteristic current distribution. The dimensional parameters are listed in Table 1. It is seen that the first four modes of the patch are TM_{10}, TM_{01}, TM_{11}, and TM_{20}, and the current distributions of Mode 1 (TM_{10}), Mode 2 (TM_{01}), and Mode 4 (TM_{20}) are orthogonal. Thus, a multi-antenna system based on these three modes is more easily capable of achieving good isolation. However, Mode 3 (TM_{11}) may lead to undesired coupling between antenna elements.

To suppress the current of Mode 3 and concentrate the current as much as possible in the lower half of the patch, a rectangular slot is etched as shown in Figure 2(a). Figures 2(b) and (c) show the MS curves and corresponding characteristic currents of the patch with slot. As shown in Figure 2(b), the operating frequency of Mode 4 (TM_{20}) shifts from 5.5 to 4.8 GHz, and the resonant frequencies of Modes 1 and 2 are not significantly affected. Additionally, compared with Figure 1(c), the current of Modes 1 and 2 in the lower half of the patch is stronger, while that of the undesired Mode 3 is weakened.

To excite Modes 1, 2, and 4 simultaneously, a coaxial probe is set at the lower half of the patch as shown in Figure 3(a). The dimensional parameters of the optimized antenna are also listed in Table 1. Figure 3(b) shows $|S_{11}|$ of the antenna element. Three operating frequency bands ($|S_{11}| < -10$ dB) of 2.56–2.64 GHz, 3.38–3.48 GHz, and 4.8–4.9 GHz with good impedance match are obtained. Additionally, Figure 4 presents the current distributions at 2.6, 3.42, and 4.84 GHz, respec-

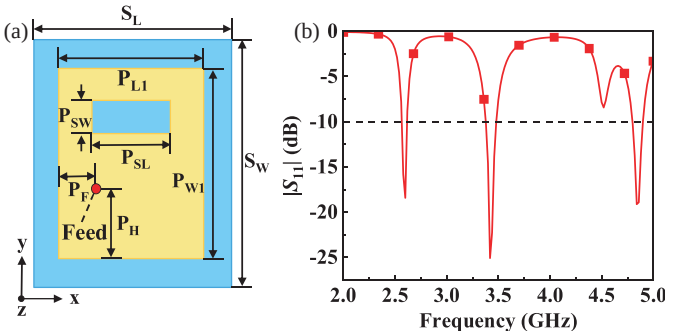

FIGURE 3. (a) Top view of the antenna element with feed and (b) the simulated $|S_{11}|$.

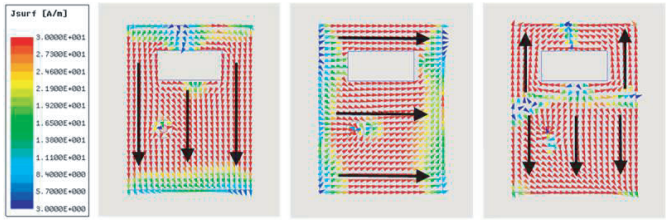

FIGURE 4. Simulated vector current distributions of single-port antenna at 2.6, 3.42, and 4.84 GHz.

TABLE 1. Design parameters of MIMO antenna.

Parameter	Value/mm	Parameter	Value/mm	Parameter	Value/mm
L_P	19	P_{L4}	14	H	1.6
W_P	25	P_{L5}	1	S	27.25
L	94	P_{W1}	25.202	S_1	31.6
W	46.5	P_{W2}	33.18	S_2	31.6
S_L	28	P_{W3}	5	S_{L1}	33.39
S_W	33	P_{W4}	3	S_{L2}	33.18
P_{SL}	10	P_{W5}	8	S_{W1}	1.83
P_{SW}	4.5	P_F	5.36	S_{W2}	2.75
P_{L1}	18.703	P_H	9.36	S_{W3}	4.125
P_{L2}	3.95	D	6.66		
P_{L3}	10	D_1	13.90		

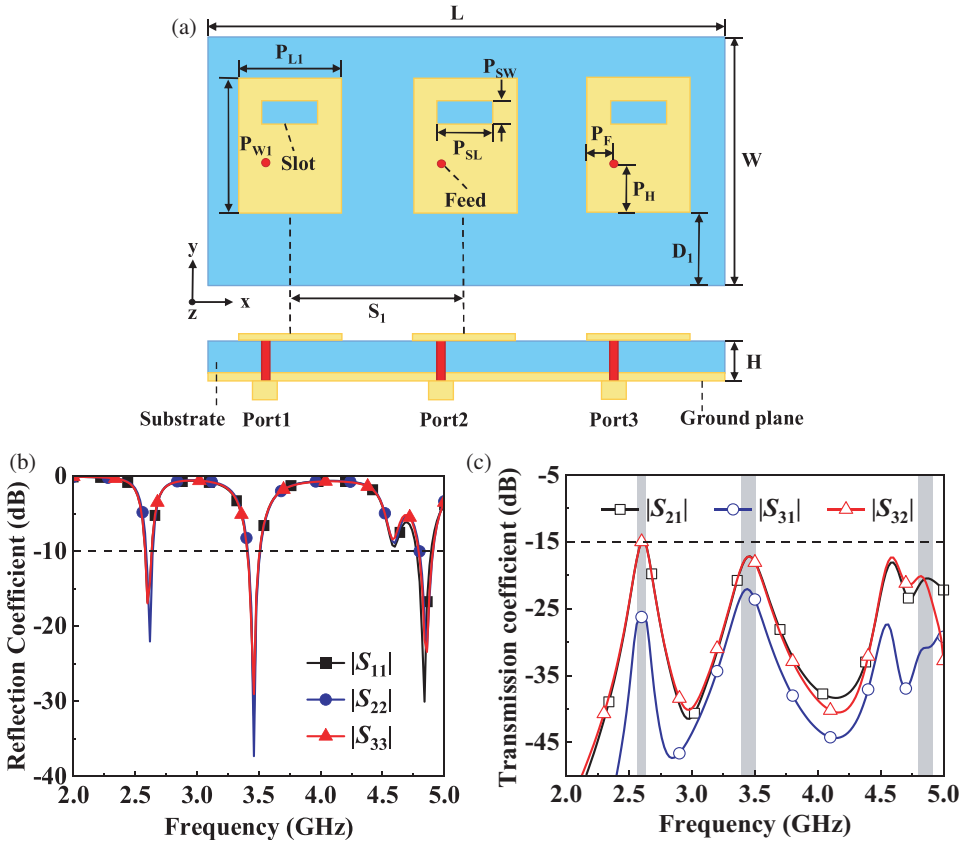

FIGURE 5. (a) Top view of the 3-port MIMO antenna, and (b) the simulated $|S_{11}|$ and (c) transmission coefficient.

tively. The current distributions are consistent with the characteristic current distributions of Modes 1, 2, and 4 in Figure 2(c), indicating that Modes 1, 2, and 4 are successfully excited.

2.2. Design of 3-Port MIMO Antenna

The antenna element is extended to a 3-port MIMO antenna by placing three elements side-by-side with the center spacing of 0.11λ (where λ is the free-space wavelength corresponding to the antenna's lowest resonant frequency) on the substrate, as shown in Figure 5(a). Figure 5(b) shows the simulated $|S_{11}|$ of the 3-port MIMO antenna. The -10 dB impedance bands are 2.57–2.64 GHz, 3.4–3.5 GHz, and 4.8–4.9 GHz, respectively, which are basically the same as that of antenna element. Figure 5(c) shows the simulated transmission coefficient of the 3-port MIMO antenna. Since the distances between two adjacent elements are the same, transmission coefficients between ports 1 and 2 ($|S_{21}|$), ports 1 and 3 ($|S_{31}|$), and ports 2 and 3 ($|S_{32}|$) are displayed here. $|S_{31}|$ at three resonant frequencies are lower than -20 dB, while $|S_{21}|$ and $|S_{32}|$ at the two lower frequencies are close to -15 dB and need to be further improved.

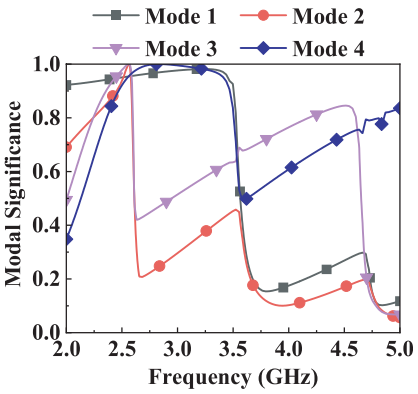

FIGURE 6. The MS curves of 3-element MIMO antenna.

3. ISOLATION ENHANCEMENT OF THE 3-PORT MIMO ANTENNA

To explore the coupling paths between adjacent ports, the significant resonance modes of each operating frequency band are analyzed by CMA, and corresponding mode current distributions are obtained.

Figure 6 shows the MS curve of the MIMO antenna. It can be observed that at 2.6, 3.42, and 4.8 GHz, the significant resonant modes (MS $>$ 0.707) are Modes 1–4, Modes 1 and 4, and Mode 4, respectively. Figure 7 shows the current distribution of the corresponding modes at the three frequency points. In Figure 7(a), at 2.6 GHz, the currents of Mode 2 are vertical, and there is current null in Mode 3 and Mode 4. Thus, they are not the main factors causing coupling. The currents of Mode 1 flow horizontally between elements, which produces coupling between them. Similarly, Mode 1 is also the root cause of coupling at 3.4 GHz in Figure 7(b). In Figure 7(c), there are many current nulls between elements such that the isolation at 4.8 GHz is high.

Since the horizontal currents on the ground plane contribute a lot to the coupling, a dual-slot DGS is introduced between adjacent antenna elements, as shown in Figure 8(a). Figures 8(b) and (c) plot the S-parameters of the antenna with and without the DGS. In Figure 8(b), the resonant frequencies of the antenna with DGS keep the same as that without DGS. Besides, in Figure 8(c), the isolation is improved. For example, $|S_{31}|$ at 3.42 and 4.8 GHz decreases from -22.2 and -30.9 dB to -35.5 and -39.5 dB, respectively. Additionally, $|S_{21}|$ and $|S_{32}|$ at 3.42 GHz are also reduced from -17.2 to -20 dB.

To explore the impact of the slots on the isolation, Figure 9 gives the current distributions of Mode 1 at 3.42 GHz and Mode 4 at 4.8 GHz. At 3.42 GHz, the currents flow oppositely on both sides of DGS, which cancel each other in the far field. In addition, current nulls are formed around element 2. Thus, the isolation at 3.42 GHz is improved. Moreover, at 4.8 GHz, the DGS creates new current nulls at the top and bottom sides of elements 1 and 3; therefore, the $|S_{31}|$ at 4.8 GHz decreases from -30.51 to -38.87 dB.

To further enhance the isolation at 2.6 GHz, an I-shaped patch with a band-stop performance is introduced. The structure of the I-shaped patch and setup of boundaries and ports are shown in Figure 10(a). The patch is printed on the same substrate as the MIMO antenna. Figure 10(b) shows the simulated S-parameter of the I-shaped patch. It is seen that at 2.6 GHz, $|S_{21}|$ is below -10 dB, and $|S_{11}|$ is close to 0 dB, implying that a stopband is obtained. If it is strategically placed between antenna elements, the coupling path may be blocked. Figure 11 illustrates the top and 3D views of the antenna with the I-shaped patch. The optimized parameters are also listed in Table 1.

Figure 12 plots the simulated S-parameters of the antenna with and without the patch. In Figure 12(a), the middle resonant frequency remains unchanged, and the other two operation bands change from 2.56–2.64 to 2.57–2.64 GHz and 4.78–4.9 to 4.80–4.91 GHz, respectively. In Figure 12(b), the isolation at 2.6 GHz is improved. For example, both $|S_{21}|$ and $|S_{32}|$ decrease from -15 to -23.3 dB, and $|S_{31}|$ decrease from -26.7 to -31.5 dB. Additionally, Figure 12(c) displays the current distribution of Mode 1. It is seen that current nulls are formed around the antenna elements. Besides, the currents on the patch flow in the opposite direction to the current next to it. Therefore, the far-field radiation cancels out and results in improved isolation.

Figure 13 illustrates the impact of feed position (P_F, P_H) on $|S_{11}|$ and I-shaped patch width (P_{W2}) on $|S_{21}|$ and $|S_{31}|$. In Figures 13 (a) and (b), it is observed that the value of P_F affects the impedance match at 3.42 GHz. As P_F increases from 5.36 to 9.36 mm, $|S_{11}|$ at 3.42 GHz increases from -25 to 0 dB. Besides, P_H affects the other two resonant frequencies. When P_H increases from 7.36 to 11.36 mm, $|S_{11}|$ at 2.6 GHz decreases from -10 to -18 dB firstly and then increases to -4.5 dB. Meanwhile, the highest resonant frequency shifts from 4.86 to 4.52 GHz. Considering the impact of the two parameters on $|S_{11}|$ comprehensively, the final choices for P_F and P_H are 5.36 and 9.36 mm, respectively. Additionally, in Figures 13(b) and (c), the value of P_{W2} affects the transmission coefficient at 2.6 and 4.86 GHz. As P_{W2} increases from 30.18 to 36.18 mm, $|S_{21}|$ at 2.6 GHz decreases from -12 to -25 dB firstly and then increases to -17 dB, and $|S_{21}|$ at 4.86 GHz decreases from -15 to -26 dB firstly and then increases to -22 dB. The $|S_{31}|$ exhibits a similar trend to $|S_{21}|$. After comprehensive consideration, 33.18 mm for P_{W2} is chosen.

4. RESULTS AND DISCUSSION

To validate the feasibility of the design and the accuracy of the simulation results, the 3-port MIMO antenna was fabricated and measured. Photos of the antenna sample and measuring environment are shown in Figure 14. The S-parameters were measured by using the vector network analyzer Agilent N5222A, and the radiation patterns were measured in a microwave anechoic chamber.

Figure 15 shows the measured and simulated S-parameters of the proposed MIMO antenna. It is seen that the trends of the experimental and simulated results are in good agreement except for slight frequency offset. For example, the simulated resonant frequencies shift from 2.6, 3.46, and 4.86 GHz to 2.51, 3.32, and 4.69 GHz, respectively. The main reason for the overall frequency shift is the dielectric constant error of the substrate.

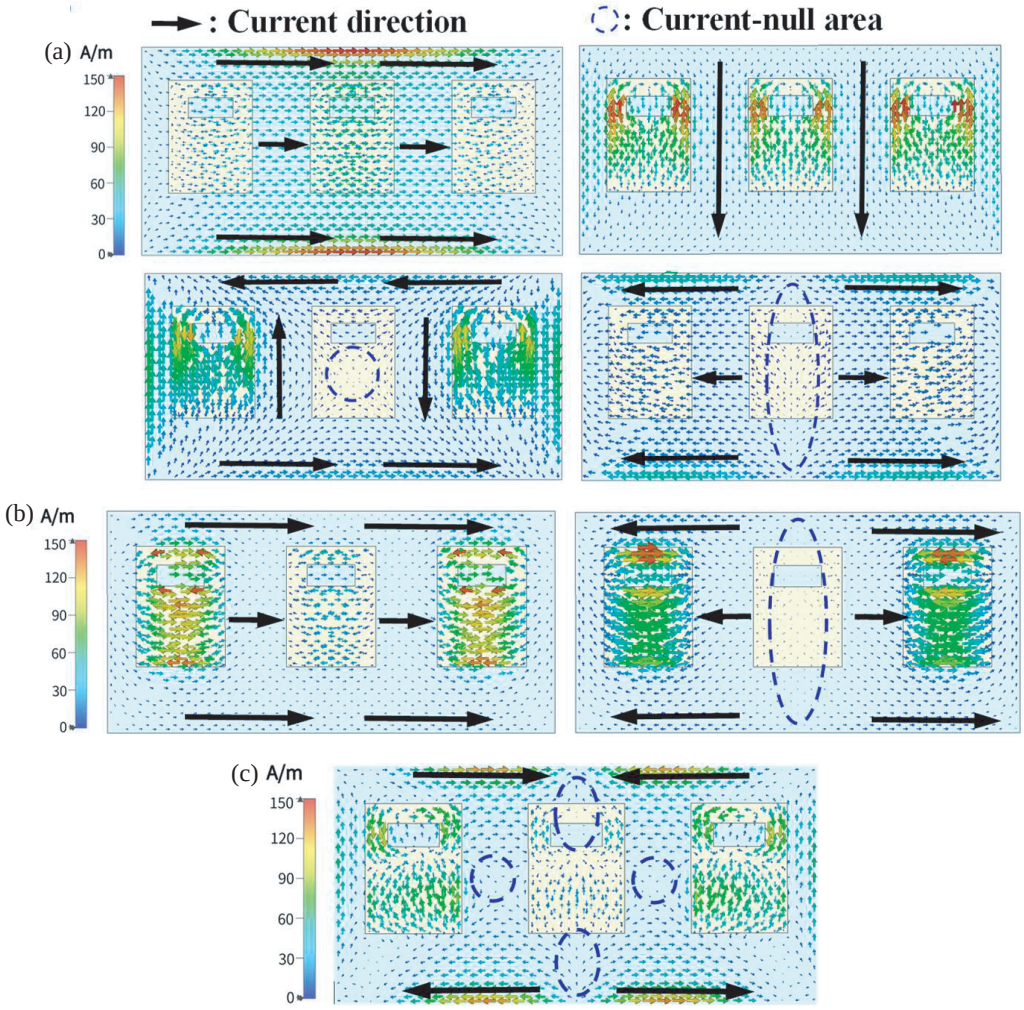

FIGURE 7. Current distribution of the main resonant modes of 3-port MIMO antenna: (a) Mode 1 to Mode 4 at 2.6 GHz, (b) Mode 1 and 4 at 3.42 GHz and (c) Mode 4 at 4.8 GHz.

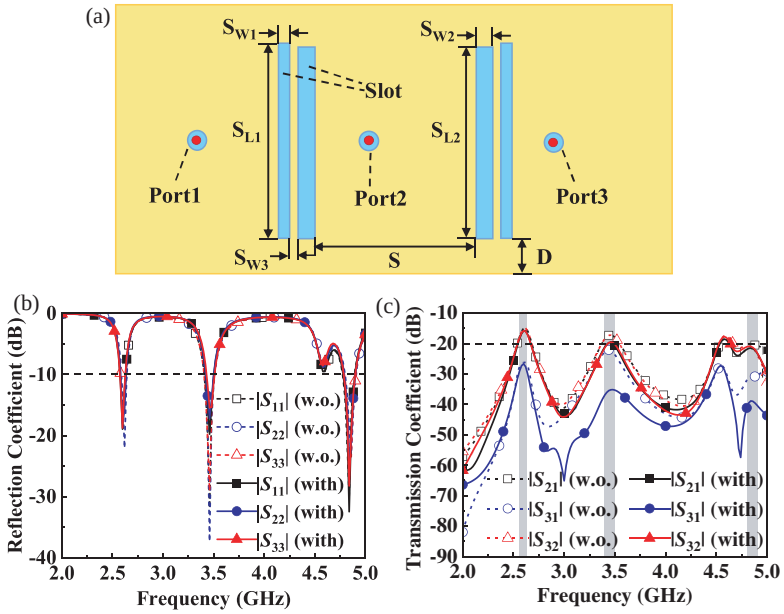

FIGURE 8. (a) Geometry and dimensions of the antenna with DGS, and (b) the simulated reflection coefficients and (c) transmission coefficients.

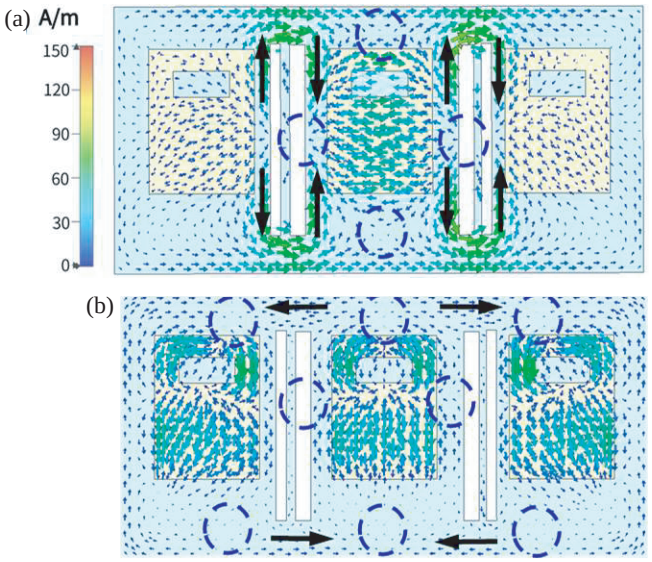

FIGURE 9. The current distribution of (a) Mode 1 at 3.42 and (b) Mode 4 at 4.8 GHz.

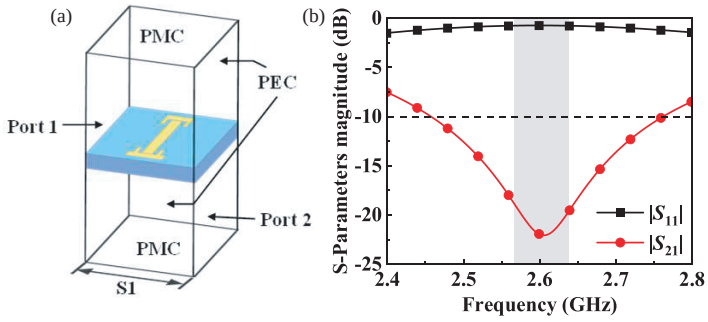

FIGURE 10. Port setting and S-parameters of the I-shaped patch: (a) Port setting, (b) S-parameters.

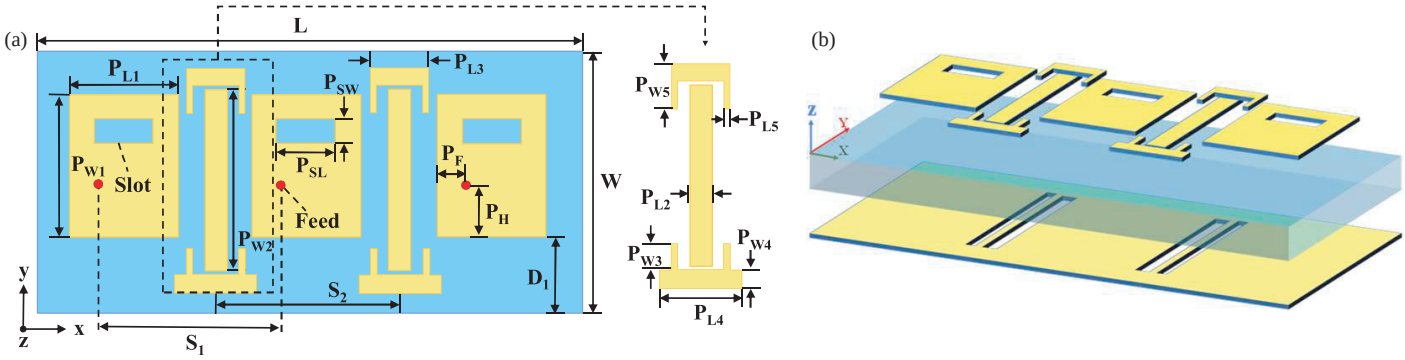

FIGURE 11. (a) The top and (b) 3D view of the proposed 3-port MIMO antenna.

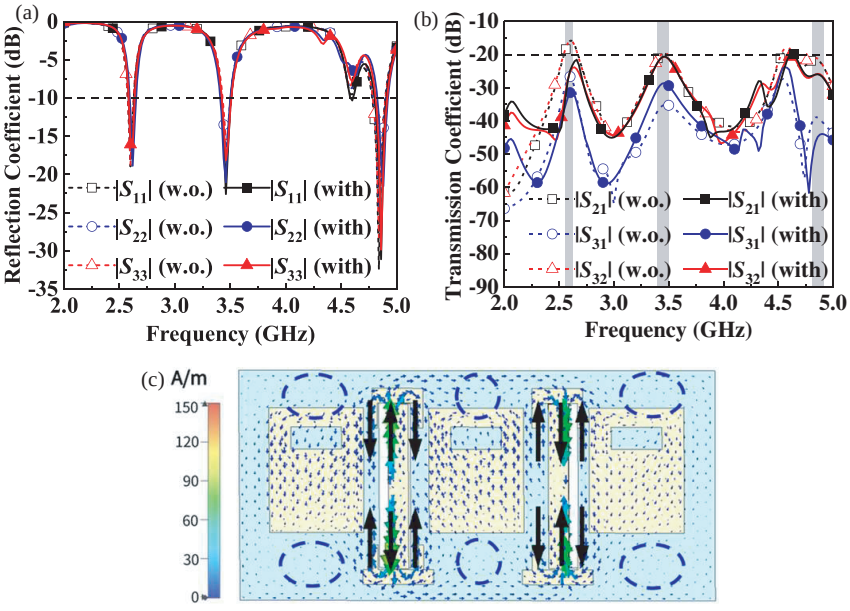

FIGURE 12. (a) The reflection coefficient, (b) the transmission coefficient with and without the I-shaped patch, and (c) the current distribution of Mode 1.

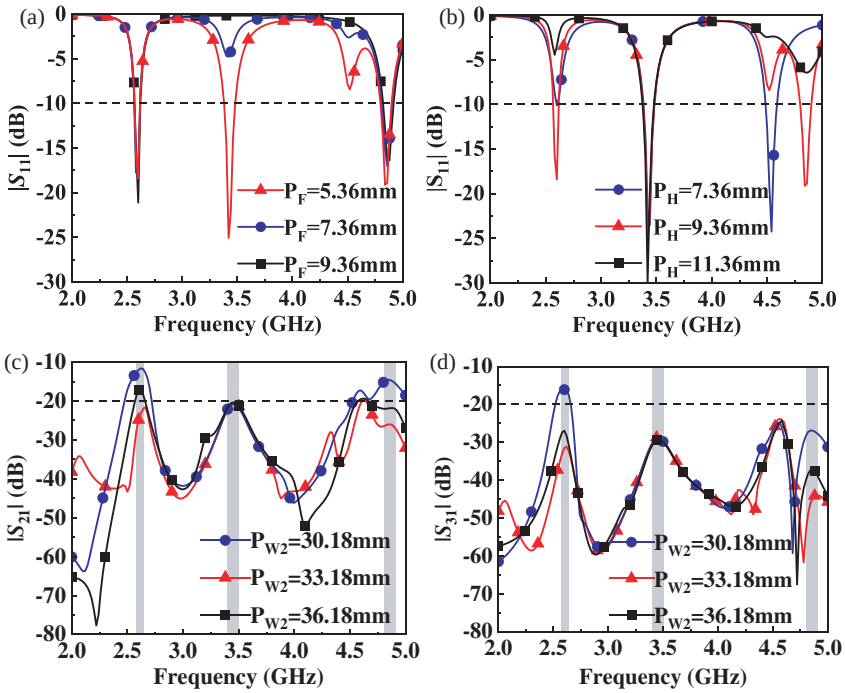

FIGURE 13. Simulated $|S_{11}|$ with different values of: (a) P_F, (b) P_H, and simulated (c) $|S_{21}|$ and (d) $|S_{31}|$ with different values of P_{W2}.

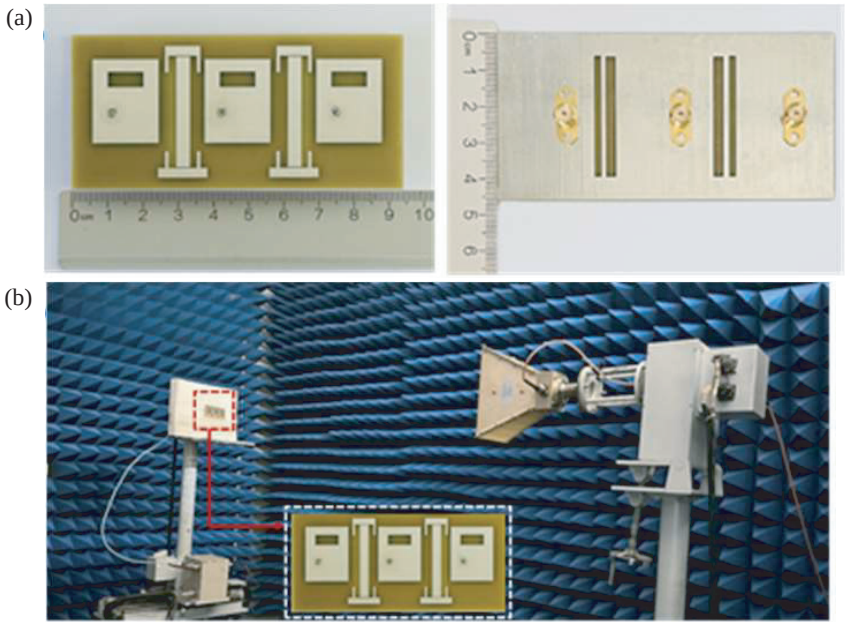

FIGURE 14. (a) Photos of the antenna and (b) the measuring environment.

Figure 16 shows the simulated and measured normalized radiation patterns at 2.6, 3.46, and 4.86 GHz when port 1 is excited. It is observed that the radiation pattern is almost omnidirectional at all the resonant frequencies, and the simulated and measured results agree well. The peak gains at 2.6, 3.46, and 4.86 GHz are 0.99, 2.04, and 2.33 dB, respectively, meeting the requirement of 5G wireless communication.

To further validate the diversity performance and data transmission quality of the antenna, the Envelope Correlation Coefficient (ECC), Diversity Gain (DG), Total Active Reflection Coefficient (TARC), and Channel Capacity Loss (CCL) are calculated. The acceptable values of ECC, DG, and CCL are below 0.5, above 6 dB, and less than 0.5 bits/Hz/sec, respectively. The ECC is calculated using the following formula:

$$ECC_{ij} = \frac{\left|S_{ii}^{*}S_{ij} + S_{ji}^{*}S_{jj}\right|^{2}}{\left(1 - |S_{ii}|^{2} - |S_{ij}|^{2}\right)\left(1 - |S_{jj}|^{2} - |S_{\mathrm{ij}}|^{2}\right)} \quad (1)$$

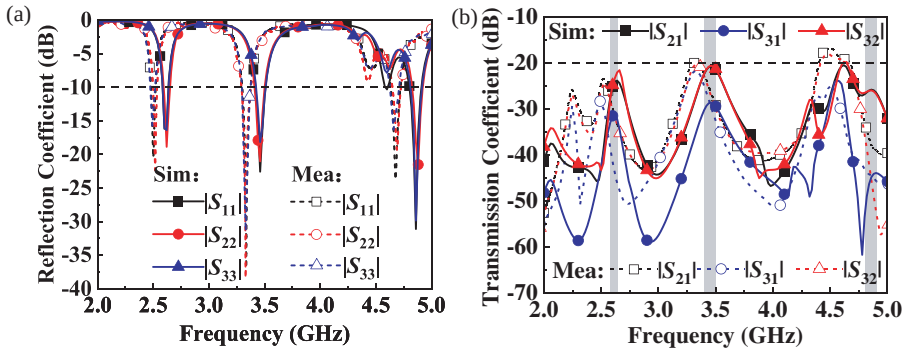

FIGURE 15. Simulated and measured S-parameter of the proposed MIMO antenna: (a) Reflection coefficient, (b) Transmission coefficient.

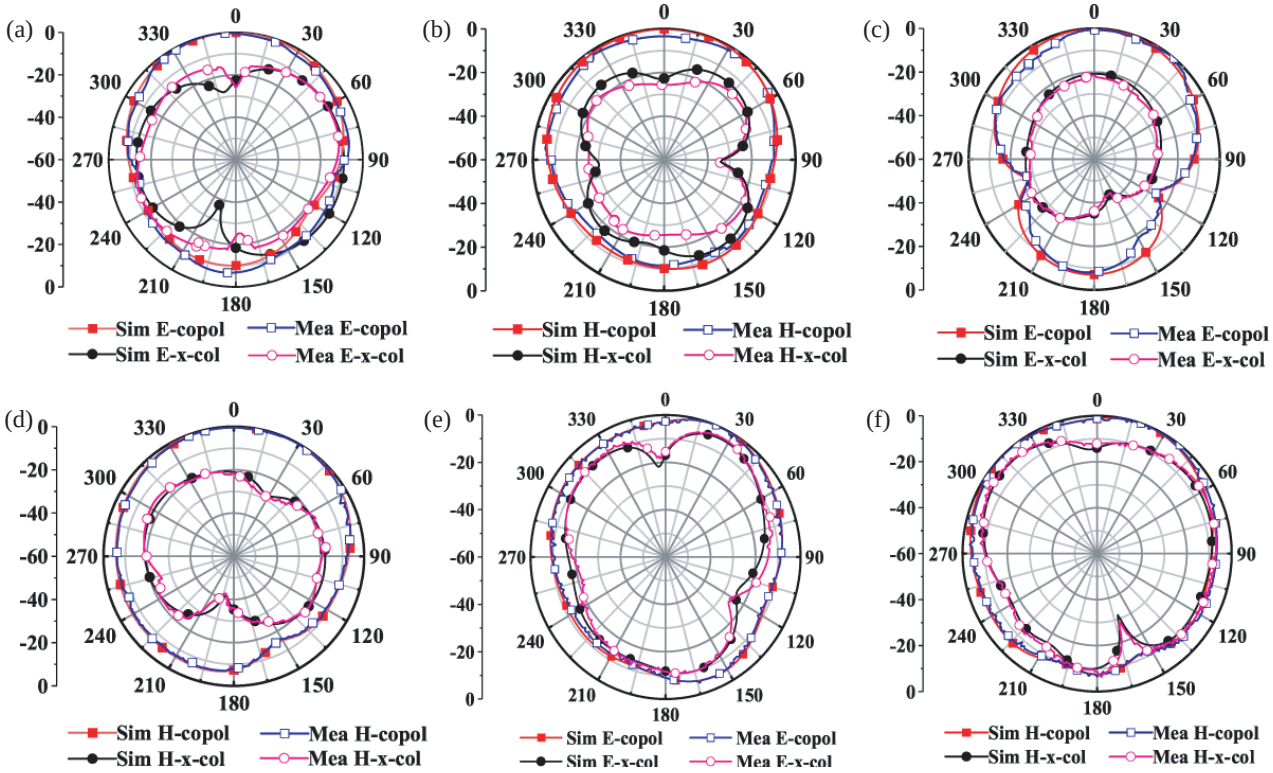

FIGURE 16. Simulated and measured normalized radiation patterns of the proposed MIMO antenna at: (a) 2.6 GHz, E-plane, (b) 2.6 GHz, H-plane, (c) 3.46 GHz, E-plane, (d) 3.46 GHz, H-plane, (e) 4.86 GHz, E-plane, and (f) 4.86 GHz, H-plane.

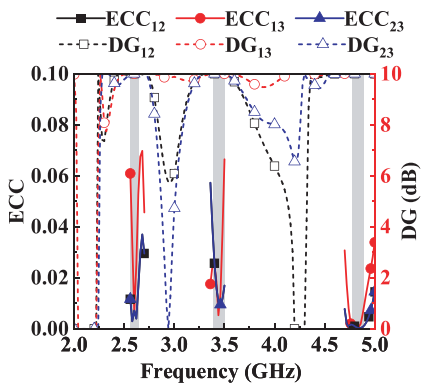

FIGURE 17. ECCs and DGs of the proposed MIMO antenna.

The DG can be calculated from the ECC. The formula is as follows:

$$DG_{ij} = 10\sqrt{1 - |ECC_{ij}|^2} \tag{2}$$

Figure 17 shows the calculated results of ECC and DG. It is observed that the ECC is less than 0.06, and the DG is above 9.9 dB in the three operating frequency bands, indicating correlation between the antenna elements and good diversity performance.

The CCL can indicate the quality of data transmission, and it can be calculated using the following formulas:

$$CCL = -\log_2 \det\left(\psi^R\right) \tag{3}$$

$$\psi^R = \begin{bmatrix} \rho_{ii} & \rho_{ij} \\ \rho_{ji} & \rho_{jj} \end{bmatrix} \tag{4}$$

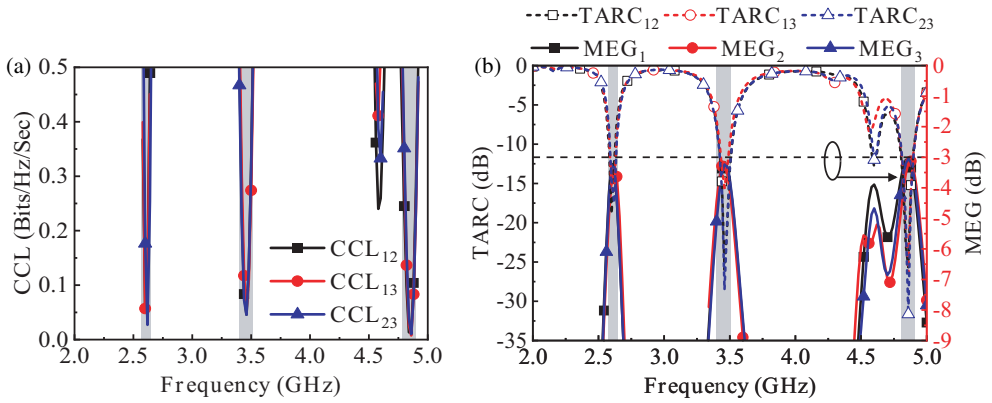

FIGURE 18. (a) CCLs and (b) TARCs and MEGs of the proposed MIMO antenna.

TABLE 2. Comparison of the performance between the proposed antenna and the other works.

Ref.	Antenna size/λ^3	Ports No.	Operating band/GHz	Element spacing/λ	Isolation/dB
[13]	$0.9 \times 0.38 \times 0.04$	2	2.25–2.63 & 5.14–6.06	0.14	> 15.3 & > 17.6
[14]	$2.4 \times 1.2 \times 0.02$	3	4.8–5.0	-	> 31
[15]	$0.95 \times 0.36 \times 0.04$	2	3.87–4.14	0.42	> 30
[16]	$1.42 \times 0.63 \times 0.01$	2	4.73–4.82	0.58	> 27
[17]	$0.97 \times 0.58 \times 0.01$	4	2.9–4.2	-	> 25
[18]	$0.28 \times 0.23 \times 0.01$	2	3.07–11.1	0.15	> 20
[19]	$3.23 \times 2.82 \times 0.02$	4	24.1–31.72	1.21	> 25
[20]	$1.45 \times 0.37 \times 0.01$	2	5.18–7.71	0.69	> 22
[21]	$0.42 \times 0.42 \times 0.03$	4	4.25–5.13	-	> 12.5
Prop.	$0.80 \times 0.40 \times 0.01$	3	2.57–2.64 & 3.4–3.5 & 4.8–4.9	0.11	> 23.3 & > 20.6 & > 25.47

$$\rho_{ii} = 1 - \left(|S_{ii}|^2 + |S_{ij}|^2\right) \tag{5}$$

$$\rho_{ij} = -\left(S_{ii}^* \times S_{ij} + S_{ji}^* \times S_{jj}\right), \ i \ and \ j = 1 \ or \ 2 \tag{6}$$

TARC is used to evaluate the overall operating bandwidth and efficiency of MIMO system, whose ideal value is smaller than 0 dB. It is calculated according to the following formula:

$$TARC_{ij} = \sqrt{\frac{\left(|S_{ii}| + |S_{ij}|\right)^2 + \left(|S_{ji}| + |S_{jj}|\right)^2}{2}} \tag{7}$$

Mean Effective Gain (MEG) is used to measure the interaction between the antenna and propagation channel. It is calculated according to the following formula [22]:

$$MEG_i = 0.5\left[1 - \sum_{j=1}^{M} |S_{ij}|^2\right] \tag{8}$$

where i, j = 1, 2, 3 represent MIMO antenna ports 1, 2, 3, respectively. In this paper, M equals 3.

Figure 18 shows the calculated CCL, TARC, and MEG. The TARC is less than -10 dB, and the CCL is less than 0.45 bits/Hz/sec within the three operating frequency bands. The results indicate that the proposed MIMO antenna has excellent data transmission quality. The MEGs are less than -3 dB and are close to each other within the three operating frequency bands, indicating that the proposed MIMO antenna can provide high-quality signal reception for the entire communication link.

To verify the novelty of this work, some previously reported designs are included for comparison in Table 2. The footprint and profile of this work are relatively small. For example, the antenna profiles in [16, 17, 20] are as small as that of this work; however, their footprint is larger. The work in [21] has the smallest footprint, but the isolation is not high, and the processing is complex. The self-decoupling methods in [13–15] need large space, and the decoupling network in [19] is not easy to design. In a word, this work achieves high isolation in three-frequency band operation with a simple structure and compact size based on CMA.

5. CONCLUSION

This paper presents a compact tri-band MIMO antenna resonating at 2.6, 3.5, and 4.8 GHz. Three orthogonal modes (TM_{10}, TM_{01}, and TM_{20}) are simultaneously excited to achieve tri-band operation and high isolation. In addition, to further enhance the isolation, the coupling paths are clearly analyzed by CMA, helping to introduce dual-slot DGS and I-shaped patch. Throughout the entire process of antenna design optimization, CMA was clearly used to explain the physical mechanisms. The designed antenna has a simple structure, compact size, and

the isolation of all three frequency bands is higher than 20 dB. The diversity performance and data transmission quality are also satisfactory, making it an excellent candidate for 5G communication.

ACKNOWLEDGEMENT

This work was supported by the National Natural Science Foundation of China under Grant 62071282, and the Natural Science Foundation of Shanxi province under Grant 202203021211295 and the Research Project Supported by Shanxi Scholarship Council of China under Grant 2024-17.

REFERENCES

[1] Sun, L., Y. Li, and Z. Zhang, "Decoupling between extremely closely spaced patch antennas by mode cancellation method," *IEEE Transactions on Antennas and Propagation*, Vol. 69, No. 6, 3074–3083, Jun. 2021.

[2] Nej, S., A. Ghosh, S. Ahmad, J. Kumar, A. Ghaffar, and M. I. Hussein, "Design and characterization of 10-elements MIMO antenna with improved isolation and radiation characteristics for mm-Wave 5G applications," *IEEE Access*, Vol. 10, 125 086–125 101, 2022.

[3] Sakli, H., C. Abdelhamid, C. Essid, and N. Sakli, "Metamaterial-based antenna performance enhancement for MIMO system applications," *IEEE Access*, Vol. 9, 38 546–38 556, 2021.

[4] Shabbir, T., M. T. Islam, S. S. Al-Bawri, R. W. Aldhaheri, K. H. Alharbi, A. J. Aljohani, and R. Saleem, "16-port non-planar MIMO antenna system with near-zero-index (NZI) metamaterial decoupling structure for 5G applications," *IEEE Access*, Vol. 8, 157 946–157 958, 2020.

[5] Li, M., L. Jiang, and K. L. Yeung, "A novel wideband decoupling network for two antennas based on the Wilkinson power divider," *IEEE Transactions on Antennas and Propagation*, Vol. 68, No. 7, 5082–5094, Jul. 2020.

[6] Li, M., M. Wang, L. Jiang, and L. K. Yeung, "Decoupling of antennas with adjacent frequency bands using cascaded decoupling network," *IEEE Transactions on Antennas and Propagation*, Vol. 69, No. 2, 1173–1178, Feb. 2021.

[7] Liu, R., X. An, H. Zheng, M. Wang, Z. Gao, and E. Li, "Neutralization line decoupling tri-band multiple-input multiple-output antenna design," *IEEE Access*, Vol. 8, 27 018–27 026, 2020.

[8] Li, M., L. Jiang, and K. L. Yeung, "A general and systematic method to design neutralization lines for isolation enhancement in MIMO antenna arrays," *IEEE Transactions on Vehicular Technology*, Vol. 69, No. 6, 6242–6253, Jun. 2020.

[9] Li, M., D. Wu, B. Xiao, K. L. Yeung, and L. Jiang, "A novel calculation method to design parasitic decoupling technique for two antennas," *IEEE Access*, Vol. 8, 116 041–116 051, 2020.

[10] Tran, H. H. and N. Nguyen-Trong, "Performance enhancement of MIMO patch antenna using parasitic elements," *IEEE Access*, Vol. 9, 30 011–30 016, 2021.

[11] Ayyadevara, M. V. N. M., B. S. N. Kishore, V. D. Midasala, and S. R. Edara, "Circularly polarized dual-frequency MIMO antenna with cosecant-squared radiation pattern for Ku-band applications," *IEEE Antennas and Wireless Propagation Letters*, Vol. 22, No. 6, 1341–1345, Jun. 2023.

[12] Kumar, P., S. Pathan, O. P. Kumar, S. Vincent, Y. Nanjappa, P. Kumar, P. Shetty, and T. Ali, "Design of a six-port compact UWB MIMO antenna with a distinctive DGS for improved isolation," *IEEE Access*, Vol. 10, 112 964–112 974, 2022.

[13] Zhang, W., Y. Li, K. Wei, and Z. Zhang, "A dual-band MIMO antenna system for 2.4/5 GHz WLAN applications," *IEEE Transactions on Antennas and Propagation*, Vol. 71, No. 7, 5749–5758, Jul. 2023.

[14] Qian, L., X. Chen, H. Zhou, H. Wang, and M. Hou, "Tri-mode dual-patch MIMO antenna with high isolation for 5G terminal applications," *IEEE Transactions on Antennas and Propagation*, Vol. 72, No. 2, 1953–1958, Feb. 2024.

[15] Lai, Q. X., Y. M. Pan, and S. Y. Zheng, "A self-decoupling method for MIMO antenna array using characteristic mode of ground plane," *IEEE Transactions on Antennas and Propagation*, Vol. 71, No. 3, 2126–2135, Mar. 2023.

[16] Tran-Huy, H., H. N. Tuan, N. Q. Dinh, D.-N. Tran-Viet, and H.-C. Park, "Multi-element self-decoupled MIMO patch antenna with flexible characteristics," *IEEE Access*, Vol. 12, 21 569–21 575, 2024.

[17] He, D., Y. Yu, and S. Mao, "Characteristic mode analysis of a MIMO antenna with DGS," in *2021 IEEE International Symposium on Antennas and Propagation and USNC-URSI Radio Science Meeting (APS/URSI)*, 1143–1144, Singapore, 2021.

[18] Shariff, B. G. P., A. A. Naik, T. Ali, P. R. Mane, R. M. David, S. Pathan, and J. Anguera, "High-isolation wide-band four-element MIMO antenna covering Ka-band for 5G wireless applications," *IEEE Access*, Vol. 11, 123 030–123 046, 2023.

[19] Li, W., L. Wu, S. Li, X. Cao, and B. Yang, "Bandwidth enhancement and isolation improvement in compact UWB-MIMO antenna assisted by characteristic mode analysis," *IEEE Access*, Vol. 12, 17 152–17 163, 2024.

[20] Jha, K. R., N. Rana, and S. K. Sharma, "Design of compact antenna array for MIMO implementation using characteristic mode analysis for 5G NR and Wi-Fi 6 applications," *IEEE Open Journal of Antennas and Propagation*, Vol. 4, 262–277, 2023.

[21] Tian, X. and Z. Du, "Wideband shared-radiator four-element MIMO antenna module for 5G mobile terminals," *IEEE Transactions on Antennas and Propagation*, Vol. 71, No. 6, 4799–4811, Jun. 2023.

[22] Addepalli, T., J. B. Kamili, S. Boddu, R. Manda, A. Nella, and B. K. Kumar, "A 4-element crescent shaped two-sided MIMO antenna for UWB, X and Ku band wireless applications," *Wireless Networks*, Vol. 29, No. 8, 3333–3348, 2023.